

Research Article

Physical Simulation and Monitoring the Deformation and Fracture of Roadway in Coal Mining

Xiaofei Liu ^{1,2}, Shuai Yang,² Xuhan Ding,³ Chong Zhang,² Xiaoran Wang,² and Bin Zhou^{3,4}

¹State Key Laboratory of Coal Resources and Safe Mining, China University of Mining and Technology, Xuzhou 221116, China

²School of Safety Engineering, China University of Mining and Technology, Xuzhou, Jiangsu 221116, China

³Department of Mining Engineering and Metallurgical Engineering, Western Australia School of Mines, Curtin University, Kalgoorlie, Australia

⁴College of Mining Engineering, Taiyuan University of Technology, Taiyuan, Shanxi 030024, China

Correspondence should be addressed to Xiaofei Liu; liuxiaofei@cumt.edu.cn

Received 2 May 2018; Accepted 31 July 2018; Published 9 September 2018

Academic Editor: Alessandro Palmeri

Copyright © 2018 Xiaofei Liu et al. This is an open access article distributed under the Creative Commons Attribution License, which permits unrestricted use, distribution, and reproduction in any medium, provided the original work is properly cited.

Aiming at the large deformation and the dynamic fracture of roadway during the underground excavation or mining, a physical simulation and strain testing system was established, and the deformation process of surrounding body and its inner strain characteristics of the simulated roadway under loading was carried out. Results showed that the inner strain change of the measurement points can be divided into three types: the strain firstly increases and then decreases, the strain slowly increases and then increases sharply, and strain firstly reduces and then increases. The strain starting time is closely related to the failure path and boundary of tested samples. This paper suggested two criteria for determining the instability of roadways, which are a huge and faster increase of strain at the location of the roof and floor with high absolute value, or a small increase with a peak value or irregular fluctuation. This paper provides a new idea for the simulation of roadway instability and is significant in deeper understanding the deformation and destabilization of underground roadway.

1. Introduction

The efficient production and transportation of coal mine cannot work without all kinds of roadway in the ground mining system. Once the deformation of roadways occurred, the normal production and transportation in mine will be seriously affected and personal casualties may even be caused. With expense of mining depth and area, the environmental and geological conditions are more complicated. The in situ stress of mining area increases associated with higher fracture frequency and intensity of roadways. Thus, the prediction and control of roadway deformation and fracture still challenges the safe mining in deep mines [1, 2]. Real-time and reasonable monitoring of roadway deformation and accurate control of surrounding rock are very

important for realizing the stability of roadway surrounding rock and ensuring the safety of roadway [3–7].

Previous studies studied the instability of the tunnel through numerical simulations and experiments (laboratory and field). Numerical simulation software verifies the roadway deformation in an ideal state which failed to consider the effect of all factors on final results [8–10]. The laboratory simulation performed better than field experiment for the isolated nuisance factors which cannot be controlled. Through monitoring the long-term deformation of underground tunnel in Jingchuan Mine and combined with the engineering geological survey, the main factors affecting the instability of the mining roadway were obtained, and the ground pressure control measures were proposed by Lu et al. [11]. Through the simultaneous

monitoring program of stress, strain, acoustic emission (AE), and ultrasonic (UT), Wang et al. [12] obtained the time and spatial relationship between stability and these parameters and proposed a joint monitoring method to detect the tunnel stability and rockburst disasters in coal mines. Chai et al. [13] used the BOTDA (Brillouin Optical Time-Domain Analysis) distributed optical fiber sensing technology to simulate the movement of rock-similar material. Based on similar simulation experiments, Zeng et al. [14] studied the failure process of deep roadway, proposed the boundary conditions of the model, and obtained the variation law of stress and strain and the failure path of the roadway model during loading. With the continuous improvement of roadway monitoring technology, optical fiber is employed for monitoring and early warning in mining industry for it directly measures the strain and temperature and indirectly measures the pressure, displacement, flow, acceleration, humidity, and other parameters. For example, the Fabry-Pérot fiber-optic sensors were used to study the hydration process in two different concrete volumes, and the results illustrated that the strain change of concrete was based on the nature of the mix and the concrete volume [15]. The microscale strain cannot be accurately determined by traditional technologies but can be monitored by the fiber-optic techniques. The very low strain in large-scale infrastructures was determined by a novel fiber-optic method, which is invented by Regez et al. [16]. At the same time, other studies [17–20] conducted the experiments in coal mine, and the results were significant to the study of monitoring deformation and fracture process of roadway by FBG.

The model test is often difficult to achieve the desired results, and accurate measurement of the internal deformation in the model test is rare. Thus, this paper establishes a similar simulation of the deformation and destruction of surrounding rock of roadway using the fiber Bragg grating sensing technology. Findings extend the existing simulation methods and offer better strategy for the investigation of the deformation and destruction of the surrounding rock.

2. Experimental Systems

2.1. Experimental System. The experimental system is composed of loading system and data acquisition system (fiber grating strain acquisition system), as shown in Figure 1. The loading system is composed of hydraulic oil pump, DCS controller, and Power Test V3.3 control program. The data acquisition system consists of FBG (fiber Bragg grating) sensor, fiber grating demodulator (America Micron Optics Company), and computer.

2.2. Experimental Program. The specimens were prepared by pulling the required amount of paraffin and sand into the mold after being dried and uniformly mixed (the mass ratio between paraffin and sand is chosen from the paper [21] by Wang et al.). They were then placed onto the bottom plate of the testing equipment as shown in Figure 1. Top load was then gradually applied to the specimen until its failure. Stress and strain data were recorded during the test.

2.3. The Model Sample Preparation. The tunnel model was made as shown in Figure 2(a). The fiber grating sensor was placed firstly in the design position, and then, the cylinder was placed in the middle of the device. The mixed sand and paraffin was put into the mold and compacted. After the paraffin was cooled, the mold was removed and placed into the loading chamber (as shown in Figure 2(b)) where the membrane stress meter was installed. According to the diameter of the round rock roadway that is 3.75 m, the diameter of similarity model was 75 mm as experimental design.

2.4. Sensor Placement. The deformation of surrounding rock is gradually expanding from inside to outside, and the study of internal deformation is a breakthrough to determine the macroscopic deformation. Therefore, in this paper, fiber Bragg grating sensing technology is used to study the internal strain characteristics of circular simulated roadway at different depths and orientations. According to the fractured image and the experimental results, the fiber grating sensor (Figure 3(a)) is selected. The radial distance of the model circular hole wall is chosen as 10 mm, 20 mm, 30 mm, and 40 mm, and the interval between each adjacent point is 45° as shown in Figure 3(b).

3. The Experiment Results of Internal Deformation of Roadway

According to the different radial distances experiment, the results of internal tunnel strain are shown in Figures 4–7.

The results show that the strain variation observed by four sensors is different as shown in Figure 4. The strain started from point 1, while the responding trends of points 1, 2, 3, and 4 are similar. Compared with the smooth variation at points 1 and 3, the strain curves of points 2 and 4 were jagged. It is noted from Figure 4(b) that the strain curves at points 5–8 were significantly different from the former ones. For example, the strain at point 8 increased rapidly at 125 s. After reaching the minimum value, the strain at point 5 also began to rapidly increase at 175 s. As a comparison, the strain change of point 7 was more stable, and point 6 had almost no change.

As shown in Figure 5, it can be seen that the change of points 1 and 3 is similar, and so do the points 2 and 4. The strain time of points 1 and 3 is earlier than that of points 2 and 4, and the value begin to rapidly increase at 140 s, after which the trend is more intense. Although the changes of points 5, 6, 7, and 8 are more complex, they are similar in the whole, and there is one impulse change of each between 100 s and 250 s, and the changes of them express as sawtooth shape from 250 s to the end of the experiment.

From Figure 6, the characteristics of strains at points 1, 4, 5, and 8 are similar. The strain at sensors 1 and 5 was observed earlier than that at sensors 4 and 8, respectively. There are no significant changes between points 2, 3, 6, and 7.

It can be seen from Figure 7 that the strain increased earlier and rapidly at points 1 and 3, and both of them reached 3000 $\mu\text{m}/\text{m}$ after 230 s. As a comparison, the strain variation at point 2 is more stable, while one peak strain

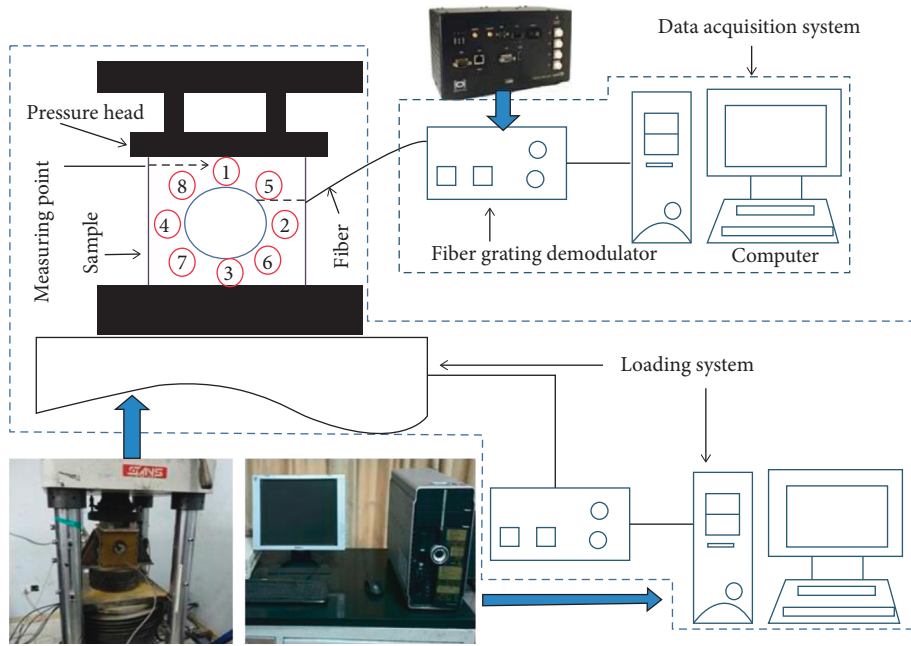


FIGURE 1: Experimental system.



FIGURE 2: Similar model sample: (a) model and (b) the sample.

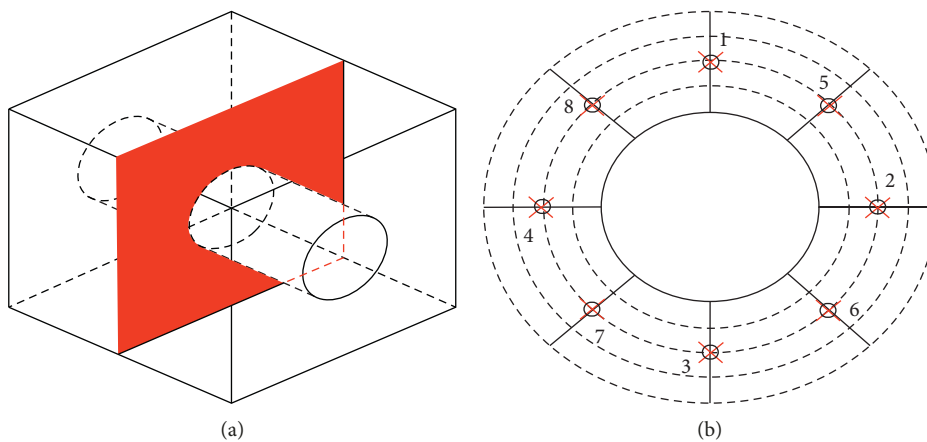


FIGURE 3: FBG sensor layout diagram: (a) grating sensor layout plane and (b) location of measuring points.

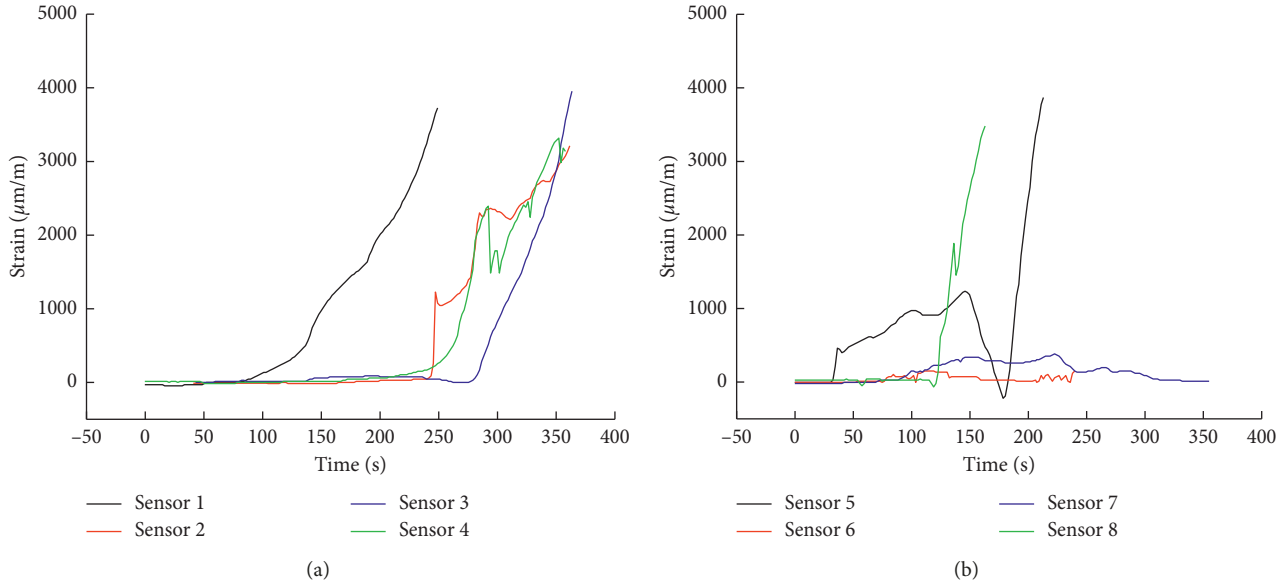


FIGURE 4: The grating strain-time curve at 10 mm from the roadway wall: (a) the strain-time curve of 1–4 FBG sensors and (b) the strain-time curve of 5–8 FBG sensors.

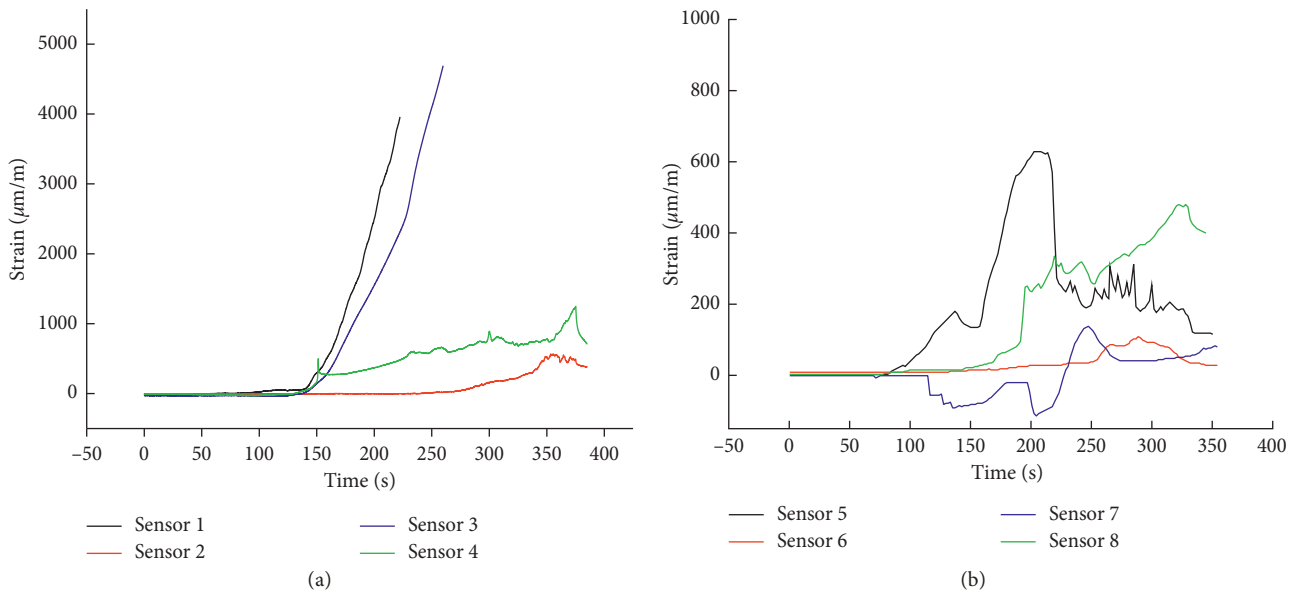


FIGURE 5: The grating strain-time curve at 20 mm from the roadway wall: (a) the strain-time curve of 1–4 FBG sensors and (b) the strain-time curve of 5–8 FBG sensors.

value $700 \mu\text{m}/\text{m}$ was observed between 200 s and 300 s at point 4. However, the strains at points 5, 6, 7, and 8 mainly change in the posttest stage. For both points 5 and 6, negative peak strain values were observed at the time 180 s and 260 s, respectively, which indicated the existence of local ruptures. The strain value at points 7 and 8 rises as vertical angle at 350 s and 410 s.

4. The Strain Law in Different Areas

The surrounding rock of roadway is divided into three regions: the cracked, plastic, and elastic regions [22], as

illustrated in Figure 8. The sample radius is r_0 , the original stress is p_0 , the support load is p_1 , and the variables subscripted 1, 2, and 3 denote rupture, plastic, and elastic zones, respectively.

Based on the equilibrium equation of the stress satisfaction in each zone (ignoring the volume force), the following equation is gained:

$$\frac{d\sigma_r}{r} + \frac{(\sigma_r - \sigma_\theta)}{r} = 0, \quad (1)$$

where σ is stress. The subscripts θ and r represent radial direction and circumferential direction, respectively.

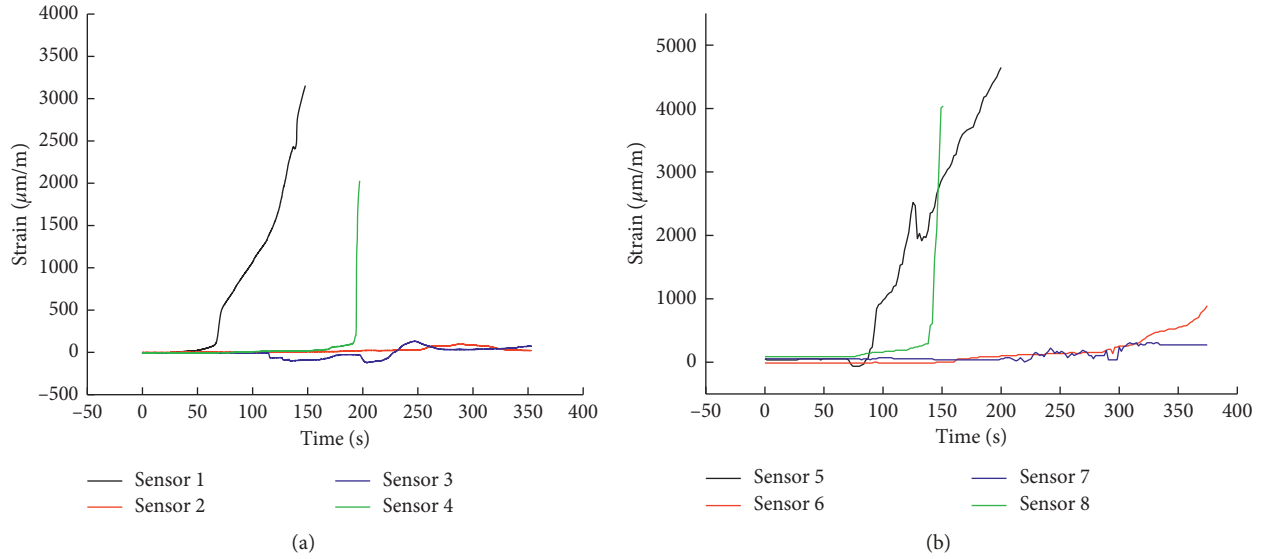


FIGURE 6: The grating strain-time curve at 30 mm from the roadway wall: (a) the strain-time curve of 1–4 FBG sensors and (b) the strain-time curve of 1–4 FBG sensors.

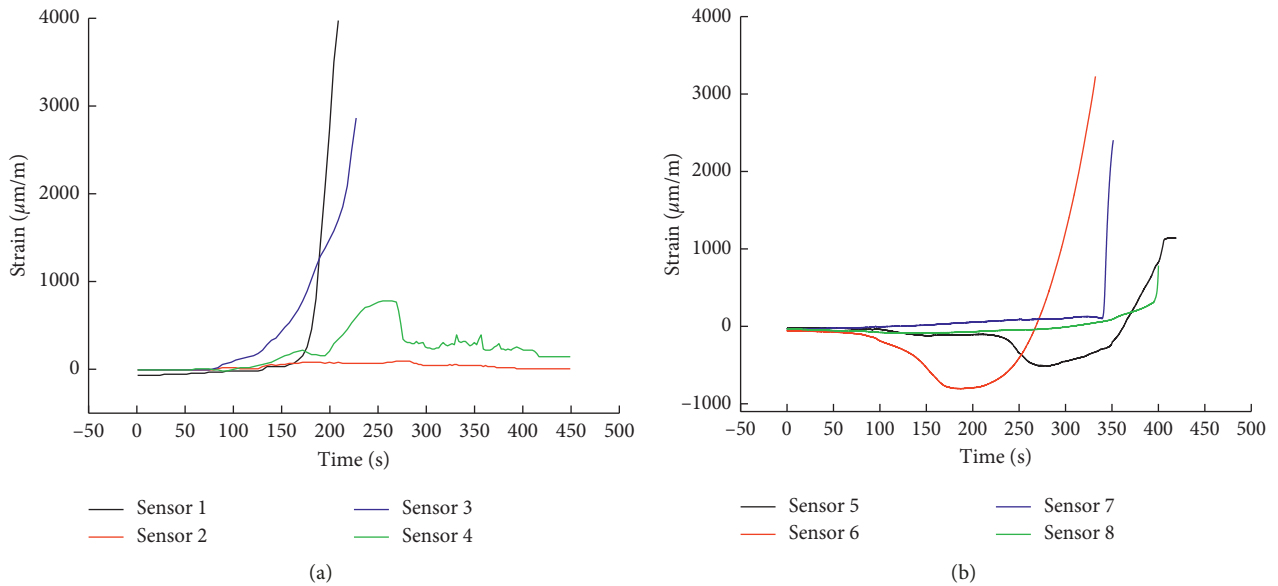


FIGURE 7: The grating strain-time curve at 40 mm from the roadway wall: (a) the strain-time curve of 1–4 FBG sensors and (b) the strain-time curve of 1–4 FBG sensors.

The stress of the surrounding rock in the presence of plastic yield and rupture satisfies the Mohr–Coulomb criterion, which can be expressed as

$$F = \sigma_{\theta} - \frac{(1 + \sin \phi)}{(1 - \sin \phi)} \sigma_r - \frac{2c \cos \phi}{(1 - \sin \phi)} = 0, \quad (2)$$

where ϕ is the internal friction angle and c is cohesion.

Based on the deformation law in each region, the following equation is gained:

$$\left. \begin{aligned} \varepsilon_r &= \frac{\partial s}{\partial r}, \\ \varepsilon_{\theta} &= \frac{s}{r}, \end{aligned} \right\} \quad (3)$$

where ε is strain and s is displacement.

According to the plasticity theory, the plastic strain depends on the plastic potential and corresponding to the Mohr–Coulomb criterion, the plastic potential Φ is obtained by the following equation:

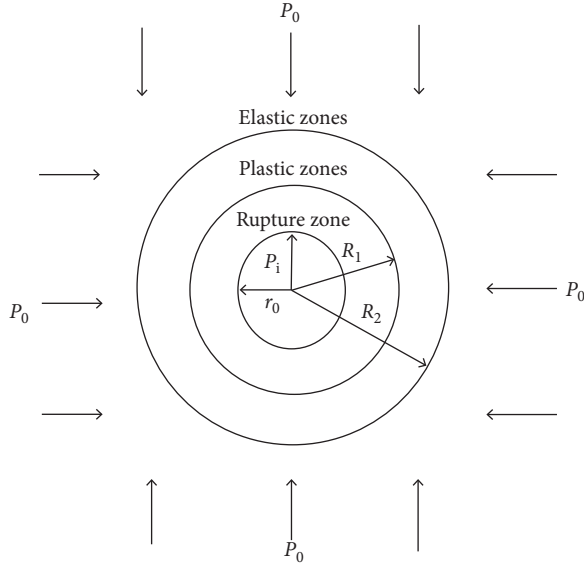


FIGURE 8: Analytic model of a circular opening.

$$\Phi = \sigma_{\theta} - \beta \sigma_r, \quad (4)$$

where $\beta = (1 + \sin \delta)/(1 - \sin \delta)$ and δ is the expansion angle.

Based on Equation (4) and nonassociated flow rules, the constitutive equation in rupture and plastic zone is expressed as

$$\left. \begin{aligned} \varepsilon_r &= \frac{[(1 - \mu)(\sigma_r - P_0) - \mu(\sigma_{\theta} - P_0)]}{(2G)} - \xi\beta, \\ \varepsilon_{\theta} &= \frac{[(1 - \mu)(\sigma_r - P_0) - \mu(\sigma_{\theta} - P_0)]}{(2G)} + \xi\beta, \end{aligned} \right\} \quad (5)$$

where P_0 is the initial stress and G is the shear modulus; μ is Poisson's ratio, and ξ is the plastic strain.

The stress boundary and contact condition of the problem are as follows:

$$\left. \begin{aligned} \sigma_{r1} &= P_i \quad (r = r_0), \\ \sigma_{r1} &= \sigma_{r2}, u_1 = u_2 \quad (r = R_1), \\ \sigma_{r2} &= \sigma_{r3}, u_2 = u_3 \quad (r = R_2), \\ \sigma_{r3} &= P_0 \quad (r = \infty), \end{aligned} \right\} \quad (6)$$

Based on the above condition and equations, the strain laws in rupture, plastic, and elastic zones are gained as shown in Equations (7)–(9).

(1) The strain law in rupture zone

$$\left. \begin{aligned} \varepsilon_{r1} &= \frac{[M_1 \eta_1 P_i^1 (r/\beta)^{M_1-1} + A \beta_1 (R_1/r)^{\beta_1-1} - (1 - 2\mu)P_0^1]}{(2G)}, \\ \varepsilon_{\theta 1} &= \frac{[\eta_1 P_i^1 (r/\beta)^{M_1-1} + A (R_1/r)^{\beta_1-1} - (1 - 2\mu)P_0^1]}{(2G)}, \end{aligned} \right\} \quad (7)$$

where $P_i^1 = c_1 \cot \varphi_1 + P_i$, $\eta_1 = (1 - \mu)(M_1 \beta_1 - 1)/(M_1 + \beta_1) - \mu$, $M_1 = (1 + \sin \varphi_1)/(1 - \sin \varphi_1)$, $\beta_1 = (1 + \sin \delta_1)/(1 - \sin \delta_1)$, $P_0^1 = P_0 + c_1 \cot \varphi_1$.

(2) The strain law in plastic zone

$$\left. \begin{aligned} \varepsilon_{r2} &= \frac{[N_2 \eta_2 \sigma_1 P_i^1 (r/R_1)^{N_2-1} + B \beta_2 (R_2/r)^{\beta_2+1} - (1 - 2\mu)P_0^2]}{(2G)}, \\ \varepsilon_{\theta 2} &= \frac{[\eta_2 \sigma_1 (r/R_1)^{N_2-1} - B (R_2/r)^{\beta_2+1} - (1 - 2\mu)P_0^2]}{(2G)}, \end{aligned} \right\} \quad (8)$$

where $\sigma_1 = P_i^1 (R_1/a)^{M_2-1} + c_2 \cot \varphi_2 - c_1 \cot \varphi_1$, $\eta_2 = (1 - \mu)(M_2 \beta_2 + 1)/(M_2 + \beta_2) - \mu$, $M_2 = (1 + \sin \varphi_2)/(1 - \sin \varphi_2)$, $P_0^2 = P_0 + c_2 \cot \varphi_2$, $\beta_2 = (1 + \sin \delta_2)/(1 - \sin \delta_2)$.

(3) The strain law in elastic zone

$$\left. \begin{aligned} \varepsilon_{r3} &= \frac{-(P_0 - \sigma_2)P_2^2 r^{-2}}{(2G)}, \\ \varepsilon_{\theta 3} &= \frac{(P_0 - \sigma_2)P_2^2 r^{-2}}{(2G)}, \end{aligned} \right\} \quad (9)$$

where $\sigma_2 = \sigma_1 (R_2/R_1)^{((1 + \sin \varphi_2)/(1 - \sin \varphi_2)) - 1} + c_2 \cot \varphi_2$.

It can be noted that the strain value decreases in radial direction and increases in circumferential direction with the distance increasing, while the strain value in radial direction and circumferential direction is different at one circumference. This explains how the strain changes under the load. However, the actual change of strain at different measuring points needs to be judged by the experimental result.

5. Discussion

5.1. The Characteristics of Strain at Different Points. Due to the influence of excavation, the original stress state at the roof and floor of the tunnel is changed from the steady state to the stress concentration state and finally reaches the new stress stabilization state. During this transaction, the sample produces secondary cracks and new cracks, and the original cracks are closed at the same time. At this point, the shape of the sample may be expanded or compressed and may be transferred from elasticity to plasticity and macroscopic rupture. As the FBG is applied as the carrier of probe, FBG will be stretched and shrunken during the loading process, so the strain value will appear positive and negative values. The strain value at point 7 in Figure 5 and points 5 and 8 in Figure 7 is negative, which means that regions are compressed under pressure. The strain value at points 1 and 3 in Figure 4 and points 4 and 8 in Figure 6 is positive, which means that the specimen is stretched under the stress. With the increases of axial load on specimen, the strain of the different probes varies. The types of the strain can be divided into three categories: Firstly, with the increase of the load, the strain firstly increases and then decreases. Secondly, the

strain increases continually during the whole loading process. In detail, the growth rate is slow at the beginning, and then at a certain moment, the strain increases exponentially. The last category is that the strain of the specimen decreases and then increases. As shown in Figures 4–7, the point 4 in Figure 7 and the point 5 in Figure 5 belong to the first type, while the point 1 in Figure 4 and the points 1 and 3 in Figure 5 belong to the second type. Surely, some points belong to the third type, such as points 5 and 6 in Figure 7. From Figure 9, during the loading process, the top of the specimen bent to the free surface after loading is greater than the degree of compaction, which is shown as type 1. Under the axial stress, as the measuring point in the rupture zone is close to the direction of the wall and principal stress, the strain is negative and gradually decreases because the cracks and pores inside the specimen are compacted during the loading process. On the other hand, the sample is bent toward free surface that causes the strain value to be greater than zero and gradually increasing. At the early stage, the effect of them is basically equal, which causes the strain to remain essentially unchanged. However, with the increase of the load, the structure gradually loses the carrying capacity which resulted in higher strain rate that increases rapidly until the sample ruptured, and this change is type 2. When the angle near the roof is 30° , the sample will slip. When be obstructed at the axis of the roadway, the structure near it will be compacted. Due to the confining pressure, the pore at the bottom of the sample will be gradually compressed. When the compaction limit is reached, the confining pressure hinders its lateral expansion, resulting in a kick drum phenomenon, manifested as type 3. Due to the uneven distribution of internal porosity and structure of the sample, different probes of the sample showed the localized rupture characteristics.

5.2. Relationship between Initial Strain Time and Final Macrofracture Mode. Figure 10(a) shows the initial time (moment) when the strain changes significantly of different monitoring points in Figures 4–7. The initial time of strain is important information to reflect where the sample will rupture. In order to make a comparison between the initial times of monitoring points and the final macrofracture of the specimen, we extract these initial times and draw this color map as shown in Figure 10(a).

As there is a hole existed at the middle of the sample with no strain, the start time of its strain is set to a longer time (longer than the rupture time). In this paper, Surfer software is used to plot the start time of strain and the position into the cloud map as shown in Figure 10(a). It can be seen from the cloud map that the first response time of the sample's strain measurement point is distributed ring-shaped. Dang et al. [23] conducted experiments and numerical simulations on direct shear tests to analyze the variation of shear forces and sample inclination during loading. The distribution is shear type at the right wing and extends from the vicinity of the wall to both ends and the direction of main stress. The strain time is discontinuous at the top of the arc, and it extended to the tunnel wall and the top of the arc. When the

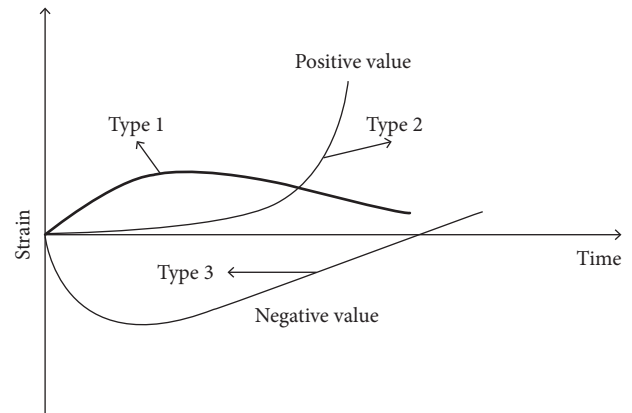


FIGURE 9: Schematic diagram of strain change type.

points at left wing and bottom are measured and the characteristics is opposite at two lower wings, the results found that the “time crack” extended from the border to the internal, and there is no obvious change at the horizontal axis before the macrofracture. However, the two lower wings became the macroscopic rupture boundary. According to the research [24–27], the stress region of both the postexcavation coal mine roadway and the loaded specimen is divided into the elastic zone and plastic zone with ring-shaped distribution and other zone, and thus, the first response time of the strain measurement point is presented ring-shaped distribution basically. As the load on the specimen increases, the radius of plastic area continues to expand, which provides a channel for crack extending. As the original structure of the right wing is weak, the structure is damaged under load, and the secondary and new cracks occur in this process. Those cracks extend to the two ends in the shear type and expand to the main stress at the same time. The area of the top of arc is obstructed by the two wings, which causes that it failed to extend horizontally and resulted in the formation of the vertical cracks which extend to both ends. As the region of horizontal axial is in force balance state and the internal structure is stable, the sample is not compacted to cause secondary cracks. Due to the squeezing force from both ends, the bottom structure is broken and extends to the free face. Therefore, the nephogram shows the law of the strain time and position and reflects rupture path and boundary of the specimen at the same time.

5.3. Scale Effect of the Physical Simulation. The scale effect means that the physical and mechanical properties of rock materials are not constant, and it changes with the geometrical dimensions of the material. Scale effect is widely found in defective materials such as rock and coal. Martin [28] experimented on 13 kinds of granite square specimens with different hole diameters and obtained the experimental results as shown in Figure 11. When the diameter of the hole is less than 75 mm, the effect on the specimens' damage is more obvious which indicates that the hole diameter has strength size effect on cave wall failure. The study of Gong et al. [29] also supports this conclusion. In order to study the roadway stability, the geometrical similarity ratio usually takes 20–50. This paper is based on a real rockburst coal

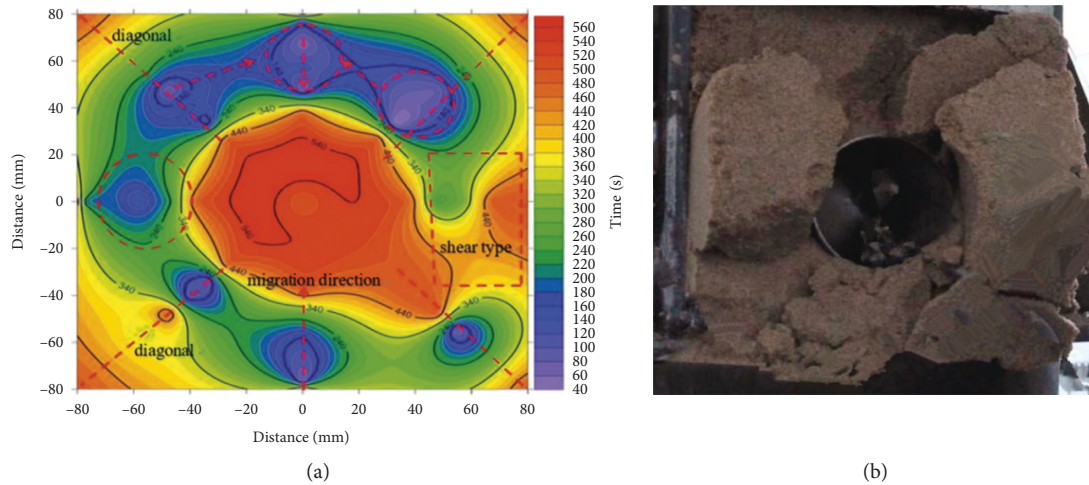


FIGURE 10: The strain-time cloud map and macrofracture figure: (a) the start time of strain and measurement points cloud map (b) the macrofracture figure.

mine and the diameter of the rock tunnel is 3.75 m. As for the design of the specimen containing hole for simulating the roadway in a real coal mine, under the premise of meeting the requirements, we optimized the scale and size of the simulated roadway and reduced section area by reducing radius of curvature. Therefore, the roadway diameter in the simulated model is designed as 75 mm. And the model similarity ratio takes 50 so that it can effectively exert the strength size effect to enhance the stability of simulated roadway.

It is absolutely correct that using merely one size or scale is not perfect in the similar simulation tests, and the size/scale effect of the model hole must be taken into account. However, due to the size limitation of the servo press machine in the simulation test, the crack propagation characterizations in the deformation and failure process of the surrounding rock in the similar simulation test are relatively difficult, and it lacks direct internal observation approach to obtain the obvious characteristics of crack development. Numerical simulation can make up for this deficiency; for example, Gao et al. [30] and Zhang et al. [31] used UDEC, ABAQUS, and other software to conduct in-depth studies on deformation and failure of roadways and instability of surrounding rock under actual size conditions. The combination of physical model and numerical simulation can complement each other at different scales. Therefore, in the further studies, on the one hand, we need to develop the internal observation approaches to obtain the crack propagation process inside through the similar simulation tests considering its size effect. On the other hand, we are supposed to carry out large-scale refined numerical simulation to provide basic model parameters and complement different scales with similar models.

5.4. Judgement on Tunnel Instability. Based on the study, the distance determines the plastic zone and the final time of rupture [32]. Therefore, the strain at 40 mm away from tunnel wall was used to judge the rupture.

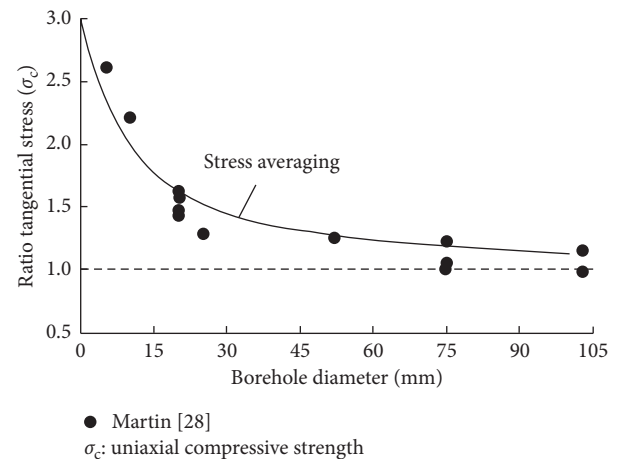


FIGURE 11: Tangential stress required to cause borehole fracture.

From Figure 12, it can be seen that the strain at points 1 and 3 increases rapidly at about 175 s and existed for 30 s, which is due to the optical fiber fracture. Strain at point 4 has a slight pulsed signal fluctuation when close to failure and then tends to be stable. The strain signal of points 5 and 6 appears to be negative at the loading stage, which indicates that there is a certain degree of internal squeezing in this place. The points 6 and 7 lose signal at the loading stage and the critical destruction stage. Strain at points 5 and 8 increases at the failure stage, with a peak value lower than 2000, which may be due to the influence of the damage in the vicinity of the damage point during and after damage stage.

It can be found that the strain at the measuring point of the roof and floor is usually increased rapidly at the beginning of the loading stage and lost signals before the critical point at the destructing stage. In other locations, the strain of the measuring point increases first and then decreases at the loading stage and tends to be constant in the destruction phase. Based on the analysis of the experimental results, the following conditions for judging the instability of

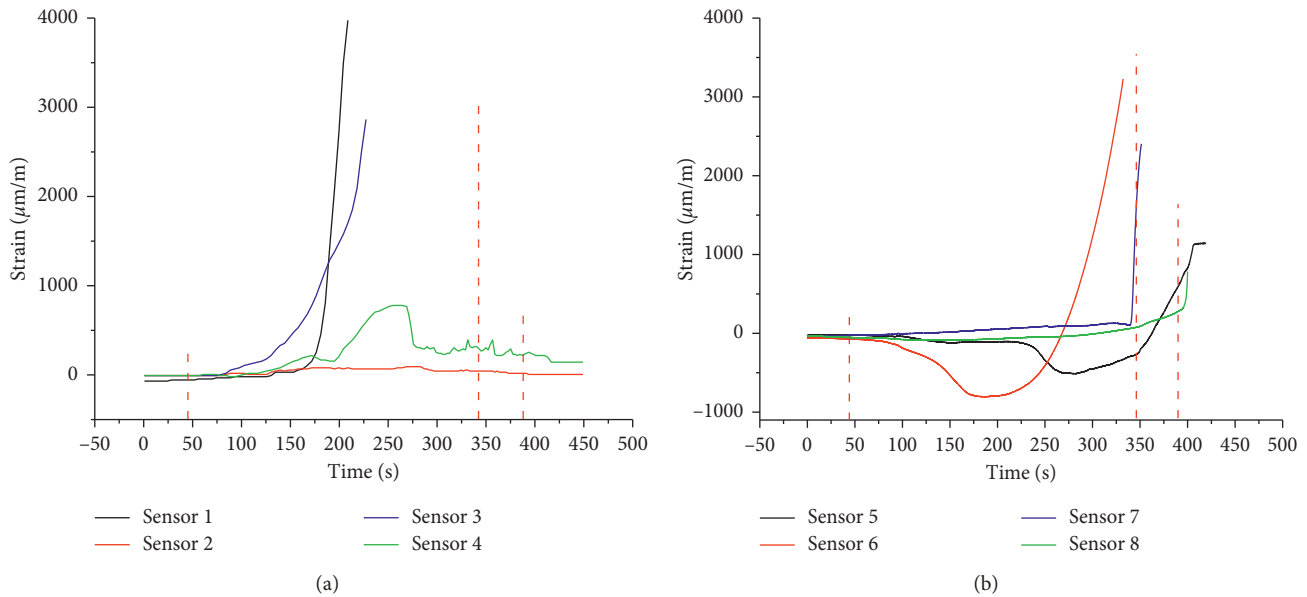


FIGURE 12: Strain time phases of 40 mm from the wall of roadway: (a) the division of strain stage of points 1–4 and (b) the division of strain stage of points 5–8.

sample are put forward. (1) The strain value at the roof and floor of the roadway starts to increase more rapidly with an absolute value of over 4000 $\mu\text{m/m}$, or the strain value increases rapidly in a short time. (2) The strain value increases a bit and then decreases with irregular fluctuation.

6. Conclusion

In this paper, we established a simulation to study the strain change of sample representing the actual tunnel. The strain time and trend are analyzed, and the conditions of instability of the tunnel are explored.

- (1) The strain of the different measurement points can be divided into three kinds, which are as follows: the strain firstly increases and then decreases with higher load, the strain increases continually throughout the loading stage with higher increasing rate, and the strain decreases firstly and then increases with higher load.
- (2) The initial time of strain is important information to reflect where the sample will rupture, and where is the rupture boundary. By comparing the cloud map with macrorupture figure, it can be seen that there is a certain relationship between the fracture path of specimen and the initial strain time. The weak structure causes the local rupture, which determines the final form under load.
- (3) The criteria of determining the instability of tunnel include the bending tensile strain at the roof and floor of the tunnel which began to increase more rapidly with high absolute value, and the strain value increases a bit and then decreases and may associate with irregular fluctuation.

Data Availability

The data used to support the findings of this study are included within the article.

Conflicts of Interest

The authors declare that they have no conflicts of interest.

Acknowledgments

This work was supported by the project funded by the National Natural Science Foundation of China (51774280) and supported by Independent Research Project of State Key Laboratory of Coal Resources and Safe Mining, CUMT (SKLCRSM18X011). The authors are grateful to all the people who help us in this paper.

References

- [1] C. J. Hou, "Key technologies for surrounding rock control in deep roadway," *Journal of China University of Mining and Technology*, vol. 46, no. 5, pp. 970–978, 2017.
- [2] S. P. Peng, "Present study and development trend of the deepen coal resource distribution and mining geologic evaluation," *Coal*, vol. 2, pp. 1–11, 2008.
- [3] S. R. Xie, M. M. Gao, D. D. Chen et al., "Stability influence factors analysis and construction of a deep beam anchorage structure in roadway roof," *International Journal of Mining Science and Technology*, vol. 28, no. 3, pp. 445–451, 2018.
- [4] C. Li, H. J. Su, and L. Hu, "Stability and support analysis of the deep extremely soft roadway," *Coal Safety*, vol. 43, no. 1, pp. 156–159, 2012.
- [5] J. P. Zuo, W. Xu, J. Wang, D. J. Liu, and F. Cui, "Investigation of failure mechanism and model for rocks in deep roadway

- under stress gradient effect,” *Journal of China University of Mining and Technology*, vol. 47, no. 3, pp. 478–485, 2018.
- [6] L. He, B. Q. Lin, Y. D. Hu et al., “Effects of in-situ stress on the stability of a roadway excavated through a coal seam,” *International Journal of Mining Science and Technology*, vol. 27, no. 6, pp. 917–927, 2017.
- [7] K. D. Liu, Q. S. Liu, B. Liu, and G. Q. Gong, “Research on control measures and effects for roadway stability in geological anomaly zone,” *Chinese Journal of Rock Mechanics and Engineering*, vol. 30, no. 12, pp. 2486–2497, 2011.
- [8] F. Q. Gao, H. P. Kang, and J. Lin, “Numerical simulation of zonal disintegration of surrounding rock mass in deep mine roadways,” *Journal of China Coal Society*, vol. 35, no. 1, pp. 21–25, 2010.
- [9] X. B. Wang, Y. S. Pan, and W. Wang, “Numerical simulation of rockburst processes of a circular tunnel at different confining pressures,” *Journal of Disaster Prevention and Mitigation Engineering*, vol. 29, no. 6, pp. 597–603, 2009.
- [10] X. B. Wang, W. Wang, and Y. S. Pan, “Numerical simulation of the strain localization of the surrounding rock of a circular tunnel at different pore pressures,” *Journal of China coal society*, vol. 35, no. 5, pp. 0723–0726, 2010.
- [11] S. B. Lu, X. Li, J. Q. Ma, and B. Yue, “Interpretation of deformation monitoring of underground roadways and its application to No. 2 diggings of Jingchuan mine,” *Chinese Journal of Rock Mechanics and Engineering*, vol. 23, no. 3, pp. 488–492, 2004.
- [12] X. R. Wang, X. F. Liu, E. Y. Wang, C. Zhang, H. S. Jia, and D. X. Li, “The time-space joint response characteristics of AE-UT under step loading and its application,” *Shock and Vibration*, vol. 2018, Article ID 6210594, 11 pages, 2018.
- [13] J. Chai, Z. S. Wang, Q. Yuan, Y. Li, S. Wang, and T. B. Li, “Application of Brillouin optical time domain analysis in strata movement similar material simulation experiment,” *Coal Science and Technology*, vol. 43, no. 1, pp. 1–4, 2015.
- [14] K. H. Zeng, J. X. Xu, and G. F. Zhang, “Experimental research on simulation of deep tunnel destruction process,” *Metal Mine*, vol. 9, pp. 44–48, 2011.
- [15] S. Yehia, T. Landolsi, M. Hassan, and M. Hallal, “Monitoring of strain induced by heat of hydration, cyclic and dynamic loads in concrete structures using fiber-optics sensors,” *Measurement*, vol. 52, pp. 33–46, 2014.
- [16] B. Regez, M. Sayeh, A. Mahajan, and F. Figueroa, “A novel fiber optics based method to measure very low strains in large scale infrastructures,” *Measurement*, vol. 42, no. 2, pp. 183–188, 2009.
- [17] D. Y. Ning, “Development of monitoring and early warning fiber sensor of water inrush from coal steam floor,” *Journal of applied Optics*, vol. 34, no. 4, pp. 718–722, 2013.
- [18] C. D. Pion, B. Shi, G. Q. Wei, L. Yu, and E. Y. Chen, “BOTDA distributed measurement and analysis of mining overburden separation,” *Journal of Mining and Safety Engineering*, vol. 32, no. 3, pp. 376–381, 2015.
- [19] D. Zhang, P. S. Zhang, B. Shi, H. X. Wang, and C. S. Li, “Monitoring and analysis of overburden deformation and failure using distributed fiber optic sensing,” *Chinese Journal of Geotechnical Engineering*, vol. 37, no. 5, pp. 952–957, 2015.
- [20] J. Chai, B. Qiu, J. X. Liu, Y. Li, and L. Dong, “Water injection test in unconsolidated strata through deep borehole based on fiber Bragg grating monitoring,” *Journal of China coal society*, vol. 37, no. 2, pp. 200–205, 2012.
- [21] X. R. Wang, X. F. Liu, E. Y. Wang et al., “Experimental research of the AE responses and fracture evolution characteristics for sand-paraffin similar material,” *Construction and Building Materials*, vol. 132, pp. 446–456, 2017.
- [22] B. S. Jiang, Q. Zhang, Y. N. He, and L. J. Han, “Elastoplastic analysis of cracked surrounding rocks in deep circular opening,” *Chinese Journal of Rock Mechanics and Engineering*, vol. 26, no. 5, pp. 982–986, 2007.
- [23] W. G. Dang, H. Konietzky, and T. Frühwirth, “Rotation and stress changes on a plane joint during direct shear tests,” *International Journal of Rock Mechanics and Mining Sciences*, vol. 89, pp. 129–135, 2016.
- [24] W. G. Dang, H. Konietzky, and T. Frühwirth, “Direct shear behavior of a plane joint under dynamic normal load (DNL) conditions,” *Engineering Geology*, vol. 213, pp. 133–141, 2016.
- [25] N. Erarslan and D. J. Williams, “The damage mechanism of rock fatigue and its relationship to the cracking toughness of rocks,” *International Journal of Rock Mechanics and Mining Sciences*, vol. 56, no. 56, pp. 15–26, 2012.
- [26] X. F. Liu, X. R. Wang, E. Y. Wang, Z. T. Liu, and X. Y. Xu, “Study on ultrasonic response to mechanical structure of coal under loading and unloading condition,” *Shock and Vibration*, vol. 2017, Article ID 7643451, 12 pages, 2017.
- [27] Q. L. Liao, Z. S. Hou, X. D. He, W. L. Dong, and Q. B. Xiao, “Monitoring and analysis on the deformation of tunnel surrounding rock affected by faults,” *Hydrogeology and Engineering Geology*, vol. 32, no. 6, pp. 102–107, 2005.
- [28] C. D. Martin, “Seventeenth Canadian Geotechnical Colloquium: the effect of cohesion loss and stress path on brittle rock strength,” *Canadian Geotechnical Journal*, vol. 34, no. 5, pp. 698–725, 1997.
- [29] F. Q. Gong, Y. Luo, X. F. Si, and X. B. Li, “Experimental modelling on rockburst in deep hard rock circular tunnels,” *Chinese Journal of Rock Mechanics and Engineering*, vol. 36, no. 7, pp. 1634–1648, 2017.
- [30] F. Q. Gao, D. Stead, and H. P. Kang, “Numerical investigation of the scale effect and anisotropy in the strength and deformability of coal,” *International Journal of Coal Geology*, vol. 136, pp. 25–37, 2014.
- [31] Q. Y. Zhang, X. T. Zhang, Z. C. Wang, W. Xiang, and J. H. Xue, “Failure mechanism and numerical simulation of zonal disintegration around a deep tunnel under high stress,” *International Journal of Rock Mechanics and Mining Sciences*, vol. 93, pp. 344–355, 2017.
- [32] S. K. Sharan, “Analytical solutions for stresses and displacements around a circular opening in a generalized Hoek–Brown rock,” *International Journal of Rock Mechanics and Mining Sciences*, vol. 45, no. 1, pp. 78–85, 2008.



Hindawi

Submit your manuscripts at
www.hindawi.com

